Effect of Magnetic Anisotropy on the 1 H NMR Paramagnetic Shifts and Relaxation Rates of Small Dysprosium(III) Complexes

Charlene Harriswangler, Fátima Lucio-Martínez, Léna Godec, Lohona Kevin Soro, Sandra Fernández-Fariña, Laura Valencia, Aurora Rodríguez-Rodríguez, David Esteban-Gómez, Loïc Charbonnière, Carlos Platas-Iglesias

Effect of Magnetic Anisotropy on the 1 H NMR Paramagnetic Shifts and Relaxation Rates of Small Dysprosium(III) Complexes

Charlene Harriswangler, Fátima Lucio-Martínez, Léna Godec, Kevin Lohona Soro, Sandra Fernandez-Farina, Laura Valencia, Aurora Rodríguez-Rodríguez, David Esteban-Gómez, Loïc J. Charbonnière, and Carlos Platas Iglesias*

ABSTRACT: We present a detailed analysis of the ^{1}H NMR chemical shifts and transverse relaxation rates of three small Dy(III) complexes having different symmetries (C_3, D_2 or C_2). The complexes show sizeable emission in the visible region due to $^{4}F_{9/2} \rightarrow {}^{6}H_J$ transitions (J = 15/2 to 11/2). Additionally, NIR emission is observed at ca. 850 ($^{4}F_{9/2} \rightarrow {}^{6}H_{7/2}$), 930 ($^{4}F_{9/2} \rightarrow {}^{6}H_{5/2}$), 1010 ($^{4}F_{9/2} \rightarrow {}^{6}F_{9/2}$) and 1175 nm ($^{4}F_{9/2} \rightarrow {}^{6}F_{7/2}$). Emission quantum yields of 1-2% were determined in aqueous solutions. The emission lifetimes indicate that no water molecules are present in the inner coordination sphere of Dy(III), which in the case of [Dy(CB-TE2PA)]$^{+}$ was confirmed by the X-ray crystal structure. The ^{1}H NMR paramagnetic shifts induced by Dy(III) were found to be dominated by the pseudocontact mechanism, though contact shifts are not negligible for some protons. The analysis of the pseudocontact shifts provided the magnetic susceptibility tensors of the three complexes, which were also investigated using CASSCF calculations. The transverse ^{1}H relaxation data follow a good linear correlation with $1/r^6$, where r is the distance between the Dy(III) ion and the observed proton. This indicates that magnetic anisotropy is not affecting significantly the relaxation of ^{1}H nuclei in the family of complexes investigated here.

INTRODUCTION

The lanthanide ions are a unique group of elements within the periodic table characterized by their similar chemical properties. The coordination chemistry of these elements is largely dominated by the trivalent oxidation state. The trivalent lanthanide ions [Ln(III)] show very similar chemical properties,[1] which are often reflected in an isostructural series of complexes across the lanthanide series.[2,3] The main difference among the Ln(III) ions resides on the smooth and gradual contraction in ionic radius when proceeding across the series from La(III) (Z = 57) to Lu(III) (Z = 71),[4] which amounts to only ~15%.[5] As a result, the light Ln(III) ions in complexes with polydentate ligands tend to adopt higher coordination numbers (9-10) than the small ones (8-9).[6] The Ln(III) ions present [Xe]4f^{n} configurations, where n varies from 0 for La(III) to 14 for Lu(III). These two metal ions are thus diamagnetic, while the remaining members of the series show paramagnetism associated to the presence of unpaired 4f electrons.

In spite of being chemically very similar, the Ln(III) ions present very different optical and magnetic properties that are associated with their own specific electron configuration. Furthermore, the 4f orbitals are shielded from the environment by the external 5s^2 and 5p^6 electrons,[7] and therefore do not significantly participate in the formation of chemical bonds.[1] As a result, the coordination environment of the Ln(III) ion has a relatively minor impact on the optical and magnetic properties of the complex. Some Ln(III) complexes form highly luminescent complexes that emit in the visible [i. e. Eu(III) and Tb(III)] or near-infrared regions [i. e. Pr(III), Nd(III), Ho(III), Er(III) or Yb(III)]. Concerning their magnetic properties, complexes of Gd(III) are widely used in clinical practice as contrast agents for magnetic resonance imaging. The [Xe]4f^7 electron configuration of Gd(III) originates from a symmetrical ^{8}S electronic ground state, which makes this ion very efficient in promoting relaxation of active NMR nuclei in its vicinity. In MRI, the shortening of relaxation times of ^{1}H water nuclei promoted by Gd(III) is used to generate contrast. Other paramagnetic Ln(III) ions induce relaxation rate enhancements in neighboring NMR nuclei, though the shorter electron relaxation times (~10^{-13} s)[8] result in longer T_1 and T_2 relaxation times. In contrast to Gd(III), all other Ln(III) ions form complexes affording observable NMR signals. Chemists have taken advantage of this feature since the early times of NMR, as paramagnetic lanthanide complexes with Ln(III) ions other than Gd(III) were found to induce significant paramagnetic chemical shifts without causing extensive line broadening. Thus, small Ln(III) complexes were routinely used as shift reagents to aid the analysis of NMR spectra of different substrates.[9]

The use of Ln(III) complexes as shift reagents has declined over the years as the increasing magnetic field strength of NMR spectrometers provided enhanced spectral resolution. Nevertheless, Ln(III)-based paramagnetic tags are widely used for protein structure determination, as the paramagnetic shifts induced by the Ln(III) ions are dominated by the dipolar (pseudocontact) contribution,[10–12] which encodes structural information. More recently, paramagnetic Ln(III) complexes were proposed as paraCEST[13–17] and paraSHIFT imaging probes[18–20] The latter can be visualized directly in an MRI experiment thanks to the paramagnetic effect that shifts ^{1}H NMR signals of the probe well out of the region were endogenous signals are observed. In paraCEST probes, contrast is generated by saturation of an NMR signal of protons exchang-

ing with bulk water. The paramagnetism of the metal ion shifts this signal far from that of bulk water.[21] From a more fundamental perspective, Ln(III)-induced paramagnetic chemical shifts and relaxation rate enhancement effects are widely used to obtain structural information in solution.[22–26]

The paramagnetic shifts induced by Ln(III) ions are reasonably well understood,[10,22,27] though recent studies pointed some limitations on the quantitative prediction of paramagnetic shifts across the series by Bleaney's theory.[28–32] The relaxation rates induced by Ln(III) ions other than Gd(III) are generally interpreted using the Solomon-Bloembergen-Morgan theory,[33–35] which relies on the point-dipole approximation and assumes that relaxation is isotropic. Recent studies reported unusual relaxation trends across the lanthanide series, and suggested that the anisotropic contribution to relaxation may not be negligible, at least for non-symmetrical systems.[36]

Chart 1. Structures of ligands discussed in the present work.

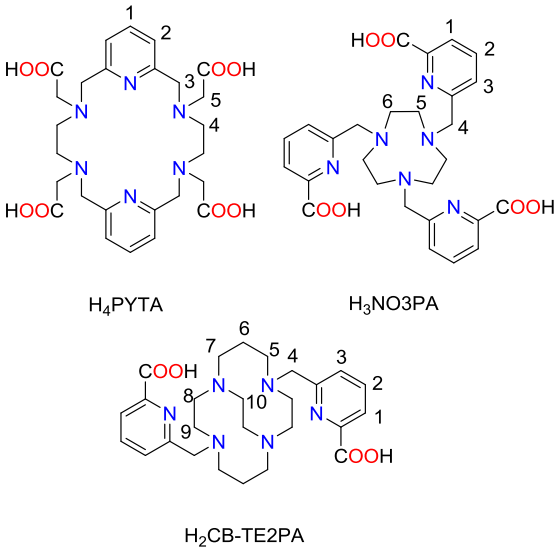

In this work, we present a detailed analysis of the ^{1}H NMR spectra of three Dy(III) complexes that provide different coordination environments. We have selected Dy(III) as a representative example of a Ln(III) ion that provides large pseudocontact shifts, actually the largest among the lanthanide series according to Bleaney's theory,[37] as well as strong relaxation enhancement effects.[38] Furthermore, the splitting of the $^6H_{15/2}$ ground state of Dy(III) can be analyzed using luminescence measurements, which can potentially provide rich electronic structure information. The three selected ligands form well characterized Ln(III) complexes. The metal ion in the [Dy(PYTA)]$^-$ complex is ten-coordinated by the ligand both in the solid state and in aqueous solution with a D_2 symmetry.[39] The H_3NO3PA ligand forms C_3-symmetrical nine-coordinate complexes that were also characterized in the solid state and in solution.[40–42] Finally, the Ln(III) complexes with H_2CB-TE2PA[43,44] contain eight-coordinate metal ions for Ln = Eu-Lu, as confirmed by the X-ray crystal structure of the Dy(III) complex reported below.

The ^{1}H NMR spectra of these complexes were measured and assigned in D_2O solutions, which allowed determining their magnetic susceptibility tensors responsible for the pseudocontact shifts, as well as estimating the contact shift contributions to the different ^{1}H NMR signals. The spectra were subsequently measured at different magnetic fields (5.88, 7.05, 9.40 and 11.75 T). The T_2 relaxation times obtained from linewidth analysis were used to test the traditional relaxation theory, as expressed by the Solomon-Bloembergen equations for the dipolar relaxation and the equations describing the Curie-spin relaxation mechanism. We demonstrate that for this series of symmetrical complexes relaxation is dominated by the isotropic contribution.

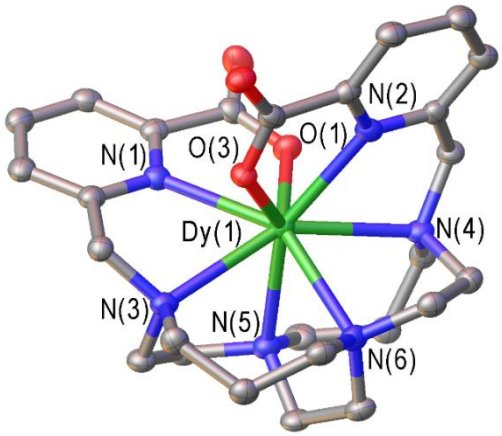

Figure 1. View of one of the [Dy(CB-TE2PA)]$^+$ units present in crystals of [Dy(CB-TE2PA)](PF_6)·2.5H_2O with ellipsoids plotted at the 30% probability level. Selected bond distances (Å): Dy(1)-O(1), 2.276(6); Dy(1)-O(3), 2.309(5); Dy(1)-N(1), 2.469(7); Dy(1)-N(2), 2.464(7); Dy(1)-N(3), 2.613(7); Dy(1)-N(4), 2.598(7); Dy(1)-N(5), 2.539(7); Dy(1)-N(6), 2.537(7).

RESULTS AND DISCUSSION

X-ray crystal structure of [Dy(CB-TE2PA)](PF_6)·2.5H_2O. Crystals of the [Dy(CB-TE2PA)]$^+$ complex suitable for X-ray diffraction studies were obtained from an aqueous solution of the complex containing an excess of KPF_6. The asymmetric unit contains two slightly different [Dy(CB-TE2PA)]$^+$ units, two PF_6^- anions and five water molecules that establish a hydrogen-bonding network with the carboxylate groups. A view of one of the [Dy(CB-TE2PA)]$^+$ units, together with bond distances and angles, are provided in Figure 1.

The Dy(III) ion resides in the interior of the ligand cleft, being directly coordinated to the eight donor atoms of the ligand. The bond distances involving amine N atoms (~2.53 – 2.62 Å) are in the low range observed for Dy(III) eight-coordinate complexes (2.54-2.68).[45–47]. The Dy-O bond distances are close to those reported for eight-coordinate complexes with polycarboxylate ligands.[45–47] The two 1,4,7-triazecane units of CB-cyclam unit adopt irregular [2233] conformations,[48] as observed previously for the La(III) and Eu(III) analogues. This is in contrast with the more common rectangular [2323] conformations observed for [In(CB-TE2PA)]$^+$ and transition metal complexes with cross-bridge cyclam derivatives.[49–51]

Photophysical properties. The absorption spectra of the [Dy(CB-TE2PA)]$^+$ and [Dy(NO3PA)] complexes (D_2O, pH 7.1-7.4) show a band with a maximum at ca. 275 nm characteristic of the picolinate chromophore (Figures S1, S2 Supporting Information).[52,53] The spectrum recorded for [Dy(PYTA)]$^-$ displays an absorption band centered at 268 nm

due to the pyridyl groups (Figure S3, Supporting Information). The emission spectra (Figure 2) recorded upon excitation through the ligand bands display the characteristic emission of Dy(III) in the visible region, with maxima around 480 ($^4F_{9/2} \rightarrow {}^6H_{15/2}$ transitions), 575 ($^4F_{9/2} \rightarrow {}^6H_{13/2}$) and 665 nm ($^4F_{9/2} \rightarrow {}^6H_{11/2}$).[54] The emission intensity in the visible region is largely dominated by the $^4F_{9/2} \rightarrow {}^6H_{13/2}$ transition at 575 nm (50-60%), as usually observed.[55–57] Additionally, sizeable emission is also observed in the NIR region of the spectrum at ca. 850 ($^4F_{9/2} \rightarrow {}^6H_{7/2}$), 930 ($^4F_{9/2} \rightarrow {}^6H_{5/2}$), 1010 ($^4F_{9/2} \rightarrow {}^6F_{9/2}$) and 1175 nm ($^4F_{9/2} \rightarrow {}^6F_{7/2}$).[58]

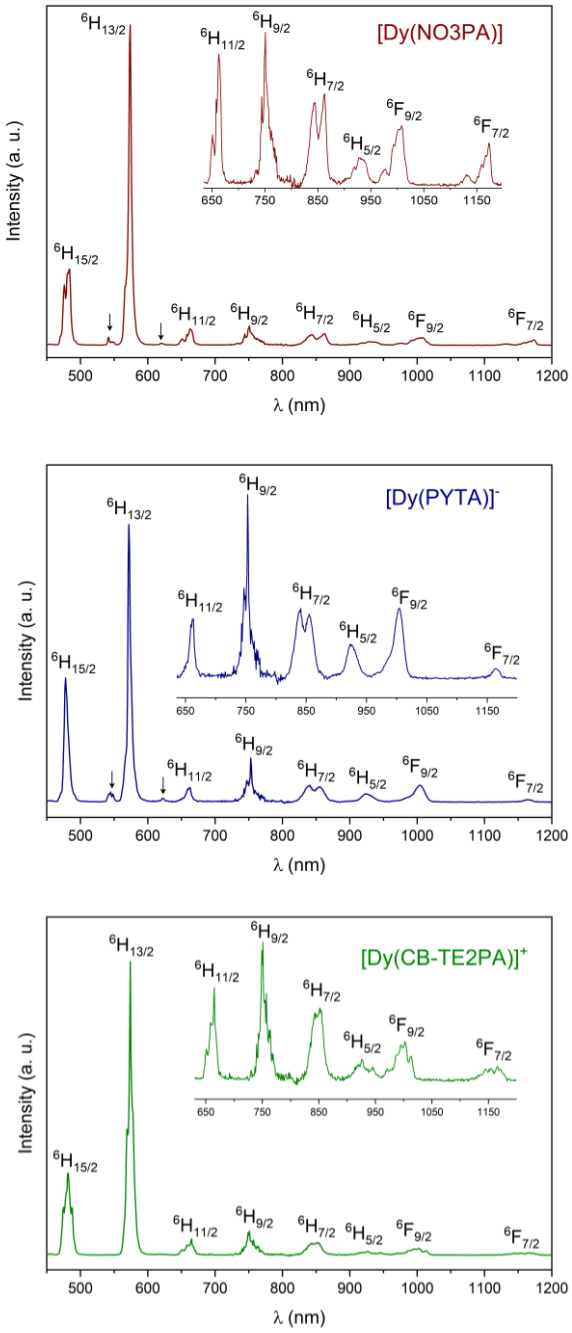

Figure 2. Emission spectra of the Dy(III) complexes recorded in D_2O solutions showing the $^4F_{9/2} \rightarrow {}^6H_J, {}^6F_J$ transitions. The arrows identify $^4I_{15/2} \rightarrow {}^6H_J$ transitions. [Dy(NO3PA)], 1.03×10^{-4} M, pD = 7.4; $[Dy(PYTA)]^-$, 1.02×10^{-4} M, pD = 7.2; $[Dy(CB\text{-}TE2PA)]^+$, 1.02×10^{-4} M, pD = 7.1.

The emission spectra recorded for the [Dy(NO3PA)] and $[Dy(PYTA)]^-$ complexes display weak emission features that are shifted ~1020 cm^{-1} to higher energies with respect to the $^4F_{9/2} \rightarrow {}^6H_J$ transitions (J = 15/2, 13/2 and 11/2). These weak emission features are attributed to transitions from the $^4I_{15/2}$ level, which lies around 1020 cm^{-1} above the $^4F_{9/2}$ level (Figure 2). The $^4I_{15/2} \rightarrow {}^6H_J$ transitions are however not observed for $[Dy(CB\text{-}TE2PA)]^+$.

The three complexes investigated here display similar lifetimes in H_2O solution, with values close to 20 μs (Table 1). These values are close to those determined in this solvent for Dy(III) complexes lacking water molecules in the inner coordination sphere (17-40 μs).[59–63] The number of water molecules coordinated to the Dy(III) ion (q) can be estimated with an uncertainty of $\pm$0.3 water molecules from these lifetimes using $q = 0.024k_{obs}$-1.3, with $k_{obs} = 1/\tau_{H_2O}$.[64] The values of q determined by this method (0.0 $\pm$ 0.2, Table 1) confirm the absence of coordinated water molecules in these complexes, in agreement with the corresponding X-ray crystal structures. The three complexes display significant differences in the lifetimes measured in D_2O (Table 1), which range from ~27 μs for $[Dy(CB\text{-}TE2PA)]^+$ to ~40 μs for $[Dy(PYTA)]^-$.

Considering the relative weakness of the NIR emission bands, they were neglected in the calculation of the luminescence quantum yields (QYs), which were determined using the visible part only. The overall QYs measured in aqueous solutions are in the range 1-2%, and roughly double in D_2O. These values are similar to those determined for Dy(III) complexes lacking coordinated water molecules (0.1-3% in H_2O),[59–63,65] with the exception of a complex with bis-tetrazolate-pyridine ligand, which shows a considerably higher ϕ_{H_2O} value of 7.1%.[66]

Figure 3 presents a comparison of the high-resolution emission spectra obtained for the three complexes at 77 K in the region of the $^4F_{9/2} \rightarrow {}^6H_{15/2}$ transition (Figure 3). The spectra recorded for the three complexes show remarkable differences in the number and energy of the different components, as well as in the overall shape of the spectrum. This indicates that the crystal field splitting of the $^6H_{15/2}$ and $^4F_{9/2}$ levels is significantly different in these Dy(III) complexes. The emission spectrum recorded for $[Dy(PYTA)]^-$ shows nine components that can be clearly identified, while the $^6H_{15/2}$ multiplet splits into eight Kramers doublets by effect of the crystal field. This suggests the emission spectrum contains contributions from hot emission bands, due to emission from different Kramers doublets of the $^4F_{9/2}$ multiplet. This situation is even more obvious in the spectrum of [Dy(NO3PA)], which shows at least nine components. The thermal energy at 77 K is ~ 53 cm^{-1}, and thus different Kramers doublets of the excited $^4F_{9/2}$ manifold may have significant populations even at this temperature. Measurements at lower temperature (4 K) would be required for a more detailed analysis. An alternative reason for the presence of hot emission bands is that they arise from the population of excited Kramers doublets of the $^4F_{9/2}$ manifold from deactivation of the $^4I_{15/2}$ manifold. This appears to be reasonable, since weak emission peaks due to $^4I_{15/2} \rightarrow {}^6H_J$ transitions are observed in the emission spectra.

Table 1. Main spectroscopic properties of the Dy complexes in water and deuterated water.[a]

	λ_{max} / nm	ε_{D_2O} / M^{-1} cm^{-1}	ϕ_{H_2O} [a,b] / %	ϕ_{D_2O} / %[a,b]	τ_{H_2O} / µs [c]	τ_{D_2O} / µs [c]	q [d]
[Dy(NO3PA)]	275	8820	2	4	20	30	-0.1
$[Dy(PYTA)]^-$	268	5450	1	2	21	40	-0.2
$[Dy(CB\text{-}TE2PA)]^+$	277	6850	1	2	18	27	0.0

[a] Measured in D_2O at pD = 7.4, 7.2 and 7.1 respectively for [Dy(NO3PA)], $[Dy(PYTA)]^-$ and $[Dy(CB\text{-}TE2PA)]^+$. [b] Calculated using Rhodamine 6G in water (ϕ_{H_2O} = 0.76),[67] estimated error ± 15%. [c] Estimated error ± 10%. [d] Calculated according to Ref. [64].

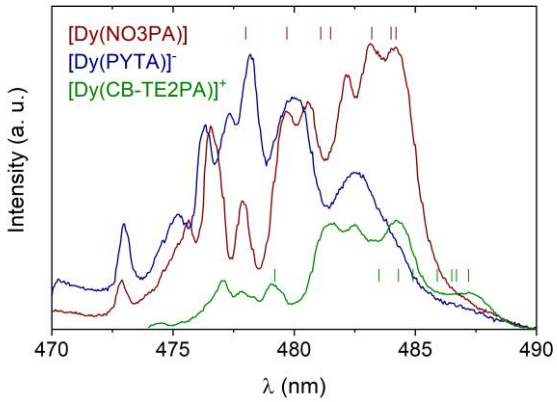

Figure 3. Emission spectra of the Dy(III) complexes recorded in frozen D_2O solutions containing 50% glycerol ($^4F_{9/2} \rightarrow {}^6H_{15/2}$ transitions). The small vertical lines show the splitting of the $^6H_{15/2}$ manifold obtained with CASSCF/QDPT calculations.

Theoretical CASSCF calculations reported previously for [Dy(NO3PA)] predicted an overall splitting of the $^6H_{15/2}$ multiplet < 300 cm^{-1} for the equilibrium geometry, though relatively small structural changes impacted significantly the energy of the Kramers doublets.[68] Our calculations performed at the CASSCF/QDPT level (see computational details below) provide a similar result, with an overall splitting of 266 cm^{-1} (Figure S4, Supporting Information). The splitting of the groups of Kramers doublets is also similar to that reported by Parker. The energies of the eight Kramers doublets are shown in Figure 3 taking as a reference the component of the emission spectrum with the lowest energy at 484.2 nm. The emission spectrum displays several components on the high energy side, out of the range marked by the splitting of the $^6H_{15/2}$ level. This again suggests that hot emission bands provide a significant contribution to the overall emission spectrum. A similar conclusion was achieved previously from the analysis of the emission spectra of Dy(III)[69] and Yb(III)[70] complexes. In the case of $[Dy(CB\text{-}TE2PA)]^+$, the splitting of the $^6H_{15/2}$ multiplet obtained with CASSCF/QDPT calculations also suggests that two components on the high-energy side arise from hot transitions. For $[Dy(PYTA)]^-$ the emission spectrum shows a broad feature on the low energy side, which makes difficult to locate the position of the Kramers doublet of the $^6H_{15/2}$ multiplet with the lowest energy. Nevertheless, CASSCF/QDPT calculations provide an overall splitting of 251 cm^{-1} for this complex, which again suggests that hot emission bands (arising from thermally-populated Kramers doublets of the $^4F_{9/2}$ multiplet) are present in the high energy side of the spectrum. Nevertheless, the emission spectra indicate that the different coordination numbers and coordination polyhedra of the three complexes have an important impact in the crystal-field splitting of the $^6H_{15/2}$ multiplet. Noteworthy, a large splitting of the $^6H_{15/2}$ manifold of about 500 cm^{-1} was observed for $[Dy(DOTA)]^-$,[71] which indicates that the splitting of the Kramers doublets is rather sensitive to variations of the coordination environment.

^{1}H NMR spectra. The ^{1}H NMR spectra of the three complexes were recorded in D_2O solution at pH ~ 7.0 (Figure 4). The ^{1}H NMR spectrum of the axially symmetrical [Dy(NO3PA)] complex displays the nine signals expected for an effective C_3 symmetry in the chemical shift range +26 to -29 ppm (at 298 K). The spectrum was partially assigned previously by Parker et al.[68] The full attribution of the spectrum was achieved using line-width analysis (Table 2), which allows identifying the axial and equatorial protons. Axial protons are generally closer to the paramagnetic center, and thus provide broader signals.[38] Noteworthy, the H5ax and H5eq protons of [Dy(NO3PA)] (Chart 1) display very similar Dy···H distances, contrary to what is observed for cyclen-based complexes. The metal ion in [Dy(NO3PA)] is placed well above the macrocycle plane (~2.05 Å according to DFT calculations, see below), as a result of the small macrocyclic cavity. In cyclen-based complexes the lanthanide resides only ~1.65 Å above the macrocycle mean plane,[72] resulting in short Dy···H_{ax} distances.

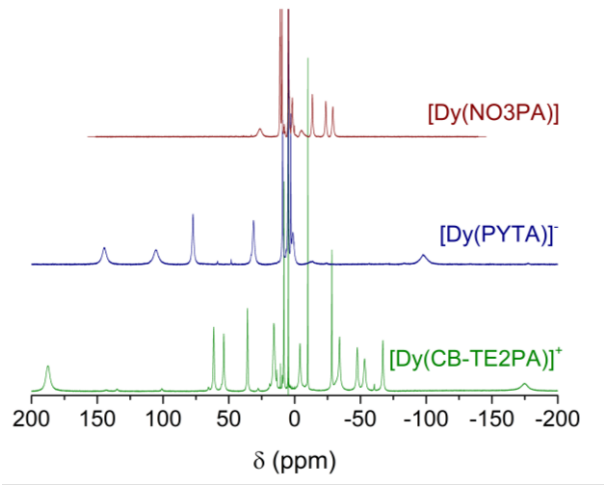

Figure 4. ^{1}H NMR spectra of the Dy(III) complexes investigated in this work (D_2O, 298 K, 300 MHz, pH ~ 7.0).

Table 2. ^{1}H NMR shifts (D_2O, 288 K, pH 7.0, 400 MHz), paramagnetic ^{1}H NMR shifts (δ^{para}) and geometric factors for the [Dy(NO3PA)] complex.[a]

	H1	H2	H3	H4ax	H4eq	H5ax	H5eq	H6ax	H6eq
δ^{obs}	9.86	10.99	11.37	28.67	1.73	-32.28	-15.05	-6.45	-25.60
δ^{para}	2.10	2.79	3.37	24.65	2.41	-35.83	-17.67	-8.66	-28.51
$(3\cos^2\theta-1)/r^3$ / 10^3 Å^{-3} [b]	-3.6543	-3.7431	-5.1772	-19.743	-2.4662	24.165	0.7444	-2.3630	9.9836

[a] See Chart 1 for labelling. Diamagnetic contributions taken from the shifts of the Lu(III) analogue, Ref. [41]. [b] Geometric factors obtained with DFT calculations (see computational methods).

Table 3. Magnetic susceptibility tensors determined from the analysis of the paramagnetic shifts of Dy(III) complexes (288 K) and CASSCF calculations.

	NO3PA^{3-}	PYTA^{4-}	CB-TE2PA^{2-}
$\Delta\chi_{ax}$ / $\times10^{-32}$ m^3	-5.5 ± 1.0	18.7 ± 0.3	-8.1 ± 0.4
$\Delta\chi_{rh}$ / $\times10^{-32}$ m^3	-	6.84 ± 0.6	21.4 ± 0.4

[a] The values obtained for the complexes with PYTA^{4-} and CB-TE2PA^{2-} were obtained including contact shifts. The principal magnetic axes in [Dy(NO3A)] and [Dy(CB-TE2PA)]$^+$ match the position of the C_3 and C_2 symmetry axes, respectively. For [Dy(PYTA)]$^-$ the *z* axes bisects the ethylenediamine units and the *x* axis contains the pyridyl N atoms.

The spectrum of [Dy(PYTA)]$^-$ presents eight signals in the range +130 to -90 ppm at 298 K, which confirms an effective D_2 symmetry of the complex in solution. A second set of paramagnetically-shifted signals corresponding to a minor species present in solution is also observed. This minor species was attributed to a complex with a nine-coordinated metal ion, in which one of the carboxylates remains uncoordinated.[39] The integration of the ^{1}H NMR signals indicates that the abundance of the minor species is ca. 10%. Finally, the [Dy(CB-TE2PA)]$^+$ complex shows 17 signals in the ^{1}H NMR spectrum, in line with an effective C_2 symmetry in solution. These resonances are observed in the chemical shift range +190 to -175 ppm.

The paramagnetic chemical shifts of Dy(III) complexes are generally dominated by the pseudocontact contribution, which can be expressed as:[10]

$$\delta^{PC} = \frac{1}{12\pi r^3}\left[\Delta\chi_{ax}\left(\frac{2z^2-x^2-y^2}{r^2}\right) + \frac{3}{2}\Delta\chi_{rh}\left(\frac{x^2-y^2}{r^2}\right)\right] \quad (1)$$

Eq (1) assumes that the reference frame coincides with the orientation of the magnetic susceptibility tensor, whose axial and rhombic contributions are given by $\Delta\chi_{ax}$ and $\Delta\chi_{rh}$, respectively. Furthermore, *x*, *y* and *z* represent the Cartesian coordinates of a nucleus *i* relative to the location of the paramagnetic metal ion [Dy(III)] placed at the origin; and $r^2 = x^2+y^2+z^2$. In Eq (1) the axial and rhombic parts of the magnetic susceptibility tensor are defined as:

$$\Delta\chi_{ax} = \chi_{zz} - \frac{\chi_{xx}+\chi_{yy}}{2} \quad (2)$$

$$\Delta\chi_{rh} = \chi_{xx} - \chi_{yy} \quad (3)$$

The three complexes investigated here present comparable Dy(III)···H distances, as demonstrated by the DFT calculations presented below. However, the chemical shift range of the Dy(III) complexes investigated here increases as the symmetry of the complex decreases, which probably reflects an increased anisotropy of the magnetic susceptibility. Alternatively, significantly different contact contributions may be responsible for the different paramagnetic shifts observed for the three complexes.

The [Dy(NO3PA)] complex is axially symmetrical, as it possesses a symmetry axis C_n with n ≥ 3. Under these circumstances, the rhombic term in Eq (1) vanishes,[73] which simplifies the analysis of the paramagnetic shifts. For axial symmetry, Eq (1) can be re-written in polar coordinates as follows:[10]

$$\delta^{PC} = \frac{\Delta\chi_{ax}}{12\pi}\frac{(3cos^2\theta-1)}{r^3} \qquad (4)$$

Thus, a plot of the pseudocontact shifts versus the geometric term $(3\cos^2\theta\text{-}1)/r^3$ should give a straight line passing through the origin with slope $\Delta\chi_{ax}/12\pi$. A plot of the observed paramagnetic shifts versus the geometric factors obtained using DFT shows a reasonable linear correlation (Figure S5, Supporting Information), affording a small $\Delta\chi_{ax}$ value (Table 3). This value is in very good agreement with that reported by Parker using ^{1}H NMR data recorded in D_2O (-5.3×10^{-32} m^3).[32]

The paramagnetic shifts observed for the $[Dy(PYTA)]^-$ and $[Dy(CB\text{-}TE2PA)]^+$ complexes were analyzed using Eq (1), with Cartesian coordinates obtained with DFT calculations. A reasonable fit was obtained using this approach, which neglects contact contributions to the paramagnetic shifts. However, we noticed that the shifts calculated for some protons with Eq (1) experience rather large deviations with respect to the observed chemical shifts, up to 22 ppm for $[Dy(PYTA)]^-$ and 31 ppm for $[Dy(CB\text{-}TE2PA)]^+$ (Table 4, see also Table S1, Supporting Information).

Table 4. ^{1}H NMR shifts (D_2O, 288 K, pH 7.0, 400 MHz), paramagnetic ^{1}H NMR shifts (δ^{para}), hyperfine coupling constants ($A/\hbar$) and contact and pseudocontact contributions calculated for the $[Dy(CB\text{-}TE2PA)]^+$ complex.[a]

	δ^{obs}	δ^{para}	$\delta^{para,calc}$	$A/\hbar$ / 10^6 rad s^{-1} [b]	δ^{C}	δ^{PC}	$\delta^{PC,calc}$
H1	-30.93	-38.32	-31.34	-0.0028	-0.77	-37.55	-32.95
H2	-11.38	-18.81	-15.98	-0.0086	-2.41	-16.40	-16.17
H3	7.72	0.88	4.36	-0.0075	-2.09	2.97	5.88
H4ax	199.63	195.69	187.4	0.0072	2.00	193.7	197.6
H4eq	57.12	52.18	74.70	0.0759	-21.24	73.43	80.28
H5ax	205.3	201.7	205.9	-0.0100	-2.79	204.5	209.7
H5eq	65.48	62.48	90.63	-0.0575	-16.09	78.57	95.10
H6ax	12.31	9.88	12.67	0.0020	0.56	9.32	15.64
H6eq	38.66	37.06	36.19	0.0026	0.71	36.35	36.81
H7ax	-18.68	-22.21	-6.42	0.0240	6.74	-28.95	-20.24
H7eq	-37.58	-40.36	-31.37	0.0310	8.67	-49.03	-34.60
H8ax	-175.9	-179.99	-171.4	0.0460	12.88	-192.9	-184.2
H8eq	-52.56	-55.08	-65.05	0.0718	20.10	-75.18	-67.18
H9ax	11.04	7.16	10.35	-0.0100	-2.80	9.96	15.31
H9eq	-5.36	-8.49	-7.50	-0.0470	-13.16	4.67	10.58
H10ax	-65.40	-68.85	-56.58	-0.0053	-1.47	-67.38	-53.08
H10eq	-78.71	-81.27	-50.39	-0.0769	-21.52	-59.75	-48.93

[a] See Chart 1 for labelling. Diamagnetic contributions estimated from the ^{1}H NMR spectrum of the La(III) analogue, Ref. [43]. [b] Hyperfine coupling constants calculated for $[Gd(CB\text{-}TE2PA)]^+$ at the TPSSh/DKH2/DKH-def2-TZVPP level (see computational methods).

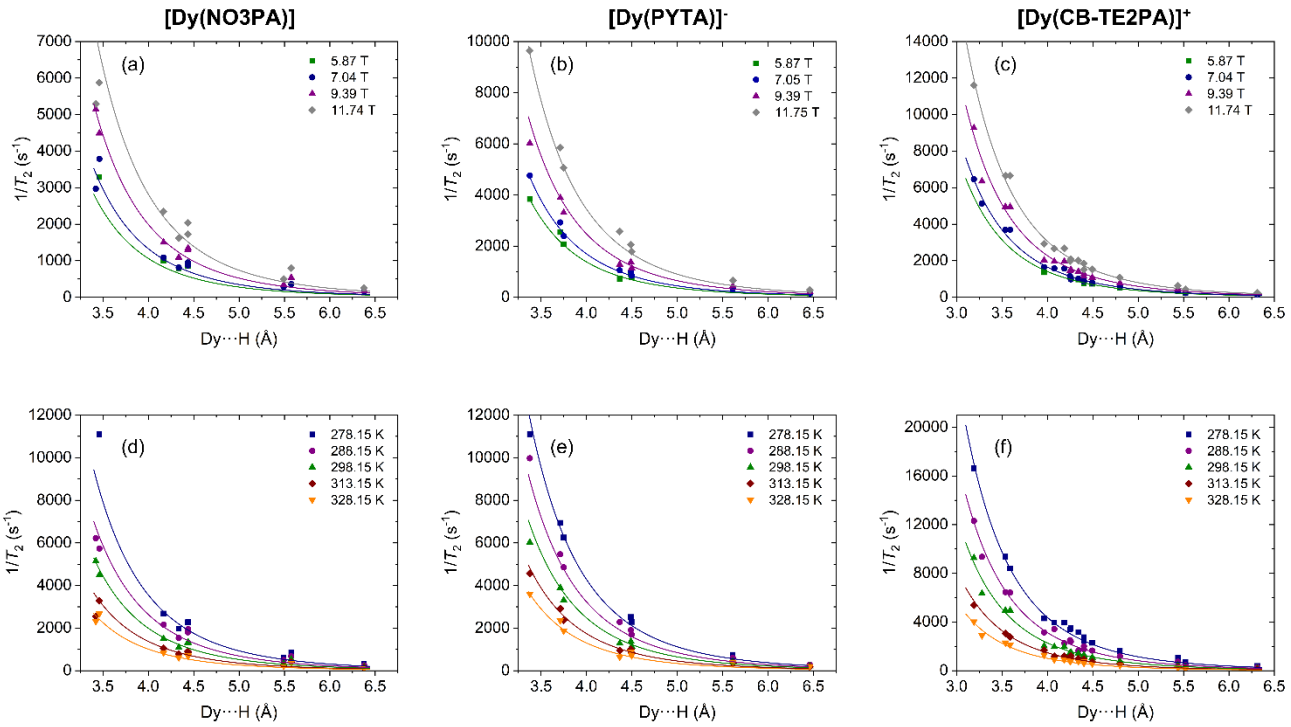

Figure 5. ^{1}H NMR transverse relaxation rates measured for Dy(III) complexes at different magnetic field strengths and temperatures (D_2O, pH ~ 7.0) versus the Dy···H distances obtained with DFT calculations. The solid lines represent the fits of the data as explained in the text.

The contact NMR shifts induced by paramagnetic Ln(III) ions are related to a through-bond delocalization of unpaired spin density of the metal ion until the observed nucleus. The spin density at the observed nucleus is given by the scalar hyperfine coupling constant $A/\hbar$, while the contact shift δ^C can be approximated by Eq (2),[22,74] where $\langle S_z \rangle$ is the spin expectation value of the lanthanide ion,[35] γ_I is the nuclear gyromagnetic ratio, k is the Boltzmann constant and β is the Bohr magneton.

$$\delta^C = \langle S_z \rangle \frac{\beta}{3kT\gamma_I} \frac{A}{\hbar} 10^6 \qquad (5)$$

Contact shifts are generally negligible for ^{1}H nuclei placed five or more bonds away the metal center, but can be significant for nuclei close to the paramagnetic ion in terms of number of bonds.[37,75] In the particular case of Dy(III), pseudocontact shifts are proportional to Bleaney's constant of C_j = -100, while the contact contribution is proportional to $\langle S_z \rangle$ (28.565 for Dy(III)).[22] Contact contributions are considered to be negligible for complexes of Yb(III), where $C_j/\langle S_z \rangle$ = 8.5, but significant for Dy(III) ($C_j/\langle S_z \rangle$ = -3.5).[26]

An estimate of the contact shifts was obtained by performing DFT calculations for the Gd(III) analogues, which provide straightforward access to the values of $A/\hbar$.[30,76,77] The results of these calculations for $[Dy(CB\text{-}TE2PA)]^+$ are presented in Table 4, while those obtained for $[Dy(PYTA)]^-$ are presented in the Supporting Information (Table S1). Contact shifts were subsequently obtained from the $A/\hbar$ values using Eq (2) and $\langle S_z \rangle$ = 22.0.[30] The results evidence that contact contributions are small for axial protons of CH_2 groups, but sizeable for equatorial protons, representing up to ~ -21 ppm for H4eq in $[Dy(PYTA)]^-$, and H4eq and H10eq in $[Dy(CB\text{-}TE2PA)]^+$. The different contact contributions observed for axial and equatorial protons reflect the Karplus-like variation of the hyperfine coupling constant with the dihedral H-C-N-Dy angle.[76]

Once contact shifts were estimated, we analyzed the pseudocontact shifts using Eq (1). The agreement between experimental and calculated shifts is very good, improving considerably with respect to the analysis neglecting contact shifts, as demonstrated by the agreement factor AF_j, defined as:[78]

$$AF_j = \sqrt{\sum_j (\delta_j^{exp} - \delta_j^{cal})^2 \,/\, \sum_j (\delta_j^{exp})^2} \qquad (6)$$

Here, the sum runs over the different proton signals observed for a given complex. The analysis performed by neglecting contact contributions affords AF_j values of 0.149 and 0.169 for $[Dy(CB\text{-}TE2PA)]^+$ and $[Dy(PYTA)]^-$, respectively, which decrease significantly to 0.091 and 0.098 upon considering the contact shifts. Similar agreement factors have been obtained for Dy(III) complexes and considered to be satisfactory.[75] These results confirm that our DFT calculations provide reasonable estimates of the contact contributions, and that the geometry of the complex obtained by DFT provides a reasonable approximation to the actual structure of the complexes.

The values of $\Delta\chi_{ax}$ and $\Delta\chi_{rh}$ obtained for $[Dy(CB\text{-}TE2PA)]^+$ and $[Dy(PYTA)]^-$ (Table 3) define rhombic magnetic susceptibility tensors, as would be expected considering the symmetry of the complexes. In the case of $[Dy(PYTA)]^-$ the axial contri-

bution is still dominant, while for $[Dy(CB\text{-}TE2PA)]^+$ the rhombic term is ca. 2.6 times larger than $\Delta\chi_{ax}$. The $\Delta\chi_{ax}$ value obtained for [Dy(NO3PA)] is about 5 times lower than those reported for Dy(III) DOTA derivatives,[79] which highlights the small magnetic anisotropy of the former. The values $\Delta\chi_{ax}$ and $\Delta\chi_{rh}$ reported for Dy(III)-DOTA derivatives are however close to those obtained here for $[Dy(CB\text{-}TE2PA)]^+$ and $[Dy(PYTA)]^-$.[80]

^{1}H NMR relaxation. Once the structures of the complexes in solution were established using paramagnetic ^{1}H NMR spectroscopy, we envisaged to investigate ^{1}H relaxation. The spectra presented above display rather broad ^{1}H NMR signals, which makes the accurate determination of T_1 relaxation times difficult. However, transverse relaxation times T_2 can be obtained from the linewidths, which can be measured with good accuracy by fitting the experimental spectrum using Lorentzian functions. The paramagnetic contribution to the transverse relaxation rates receive contributions from the dipolar and Curie spin mechanisms. The dipolar contribution T_2^D is the result of a through-space interaction between the observed nucleus and the unpaired electron spins, originating from the fluctuating magnetic field associated to electron relaxation, Eq (7):[22,33]

$$\frac{1}{T_2^D} = \frac{1}{15}\left(\frac{\mu_0}{4\pi}\right)^2 \frac{\gamma_I^2 \mu_{eff}^2 \beta^2}{r^6}\left(4\tau_c + \frac{3\tau_c}{1+\omega_I^2\tau_c^2} + \frac{13\tau_c}{1+\omega_S^2\tau_c^2}\right) \qquad (7)$$

Here, $\mu_0/4\pi$ is the magnetic permeability of a vacuum, γ_I is the nuclear gyromagnetic ratio, μ_{eff} is the effective magnetic moment of the paramagnetic ion, β is the Bohr magneton, ω_I is the Larmor frequency of the nucleus, ω_S is the Larmor procession frequency for an electron and r is the distance between the observed nuclei and the paramagnetic center. The correlation time τ_C depends on the rotational correlation time, τ_R, and the electronic relaxation time T_{1e}:

$$\frac{1}{\tau_C} = \frac{1}{T_{1e}} + \frac{1}{\tau_R} \qquad (8)$$

The Curie spin (CS) mechanism is also a dipolar effect arising from the interaction of the nuclear spin and the static magnetic moment of the electrons, associated to the difference in population of the electron spin levels due to the Boltzmann distribution:[81]

$$\frac{1}{T_2^{CS}} = \frac{1}{5}\left(\frac{\mu_0}{4\pi}\right)^2 \frac{\gamma_I^2 H_0^2 \mu_{eff}^4 \beta^4}{(3kT)^2 r^6}\left(4\tau_R + \frac{3\tau_R}{1+\omega_I^2\tau_R^2}\right) \qquad (9)$$

Inspection of Eq 9 evidences that the Curie spin mechanism is expected to become more important as the applied magnetic field (H_0) increases, particularly in the case of Ln(III) ions with high μ_{eff} values. Different authors have taken advantage of the dependence of the CS contribution with H_0^2 to estimate relative Ln···H distances, with plots of $1/T_i$ (i = 1 or 2) versus H_0^2 generally showing good linear correlations.[38,39,82,83] It is important to mention that magnetic anisotropy may play a key role in the relaxation of ^{1}H nuclei of small lanthanide complexes, with the anisotropic and isotropic parts providing similar contributions.[84] Part of the motivation of the present work was to test the traditional relaxation theory (Eqs 7-9) using a well characterized set of complexes having different magnetic anisotropies. This is the case of the complexes investigated here, as demonstrated by the data reported in Table 3.

The linewidths of the ^{1}H NMR signals of the complexes investigated here were obtained at four different magnetic fields (5.9, 7.05, 9.4 and 11.7 T) at 298 K. Furthermore, we also obtained a set of linewidths at 9.4 T and five different temperatures. We hypothesized that the variable field data would provide aid the fit of the relaxation data to Eqs (7)-(9), allowing to discriminate the contributions of the dipolar and CS mechanisms. We have chosen a set of very rigid complexes, so that line-broadening due to exchange effects provide negligible contributions to the linewidths. The measured linewidths are large (35-3600 Hz), and thus diamagnetic effects (~4 Hz) were neglected.

The relaxation rates obtained from linewidth data display reasonably good linear correlations when plotted against $1/r^6$, with distances taken from DFT calculations (Figures S6-S8, Supporting Information). These results suggest that classical relaxation theory provides a reasonably good description of ^{1}H relaxation in this family of complexes. We also note that R_2 displays a linear dependence with the square of the applied magnetic field (Figures S9-S11, Supporting Information), as expected according to Eq (6). The plots of $1/T_2$ versus the Dy···H distances also evidence that relaxation is faster upon increasing the magnetic field strength (Figure 5). The relaxation rates increase upon decreasing the temperature, which is mainly the combined effect of the $1/T^2$ dependence of the Curie spin mechanism and the increased value of τ_R due to slower rotational motion at lower temperatures.

The transverse relaxation rates were fitted to Eqs (7)-(9) assuming that both T_{1e} and τ_R display an Arrhenius dependence with temperature with activation energies E_R and E_V, respectively.[85,86] The fits are shown in Figure 5, while the fitted parameters are given in Table 5. Due to the relatively large number of parameters, we had to fix μ_{eff} to the common value of 10.64 BM.[87] Furthermore, the value of E_v were fixed to 1 kJ mol^{-1} for [Dy(NO3PA)] and $[Dy(PYTA)]^-$, as otherwise small negative values were obtained. This has been observed previously very often when investigating the relaxation properties of Gd(III) complexes.[85,88,89] Values of E_v close to 1 kJ mol^{-1} were reported for the lanthanide aqua-ions.[8]

Table 5. Parameters obtained from the fits of relaxation data for Dy(III) complexes.[a]

	$NO3PA^{3-}$	$PYTA^{4-}$	$CB\text{-}TE2PA^{2-}$
τ_R / ps	122 ± 10	150 ± 6	122 ± 4
T_{1e} / fs	196 ± 30	286 ± 39	375 ± 38
E_R / kJ mol^{-1}	21.3 ± 1.6	21.4 ± 0.9	26.2 ± 1.0
E_V	1[a]	1[a]	11.9 ± 3.6

[a] Fixed during the fitting procedure.

The values of τ_R obtained from the fits of the data are very reasonable considering the size of the complexes,[90] with the slightly longer value of τ_R being observed for the complex with the highest molecular weight. One should note that the values of τ_R obtained from ^{1}H NMRD studies on Gd(III) complexes are expected to be somewhat shorter due to the local mobility (internal motion) of the coordinated water molecule.[82] The values of E_R are also close to those determined from ^{1}H NMRD studies on Gd(III) complexes (~20 kJ mol^{-1}). For $[Dy(CB\text{-}TE2PA)]^+$ the fit of the data afforded a rather high

value of E_V (11.9 kJ mol^{-1}), as well as a high value of E_R. However, these values should be taken with some care, as these parameters are strongly correlated. It is however possible that the extreme rigidity of this complex results in a higher activation energy for the modulation of T_{1e}.

The values of T_{1e} obtained for the three complexes are relatively similar, increasing from 196 fs for [Dy(NO3PA)] to 375 fs for [Dy(CB-TE2PA)]$^+$. Very similar values were reported for the Dy(III) aqua-ion $[Dy(H_2O)_8]^{3+}$ (299 ps)[8] and for the [Dy(DOTA)]$^-$ complex (~250 fs).[38] This suggests that T_{1e} is rather insensitive to the coordination environment around the metal ion. The short values of T_{1e} suggest that electron relaxation may be modulated by fast molecular vibrations.

CONCLUSIONS

The purpose of this work was to analyze ^{1}H NMR relaxation in a series of well-characterized Dy(III) complexes. Luminescence measurements and the X-ray crystal structure of [Dy(CB-TE2PA)]$^+$ were reported here for the sake of completeness. The selected complexes display different coordination numbers and thus coordination polyhedra, which results in markedly different magnetic anisotropies, which were obtained using ^{1}H NMR measurements. The analysis of the transverse relaxation rates evidences that the Solomon-Bloembergen-Morgan theory describes reasonably well relaxation in these complexes, as evidenced by the linear dependence of $1/T_2$ with $1/r^6$. This indicates that anisotropic relaxation does not provide a significant contribution for the complexes investigated here. We note that the effect of anisotropy is expected to be small while being one order of magnitude smaller than the average susceptibility.[91] This situation is observed for the complexes investigated here, as $\Delta\chi_{ax}$ and $\Delta\chi_{rh}$ represent < 15% of χ_{iso} (~151×10^{-32} m^3). In the case of [Dy(NO3PA)], $\Delta\chi_{ax}$ is particularly small compared with χ_{iso} (< 4%). However, we do not exclude that anisotropic relaxation may play a role in Ln(III) complexes with very large magnetic anisotropies.

EXPERIMENTAL AND COMPUTATIONAL SECTION

General. All solvents and reagents used were purchased from commercial sources, had reagent grade quality and were used as supplied. Ligands NO3PA^{3-},[41] CB-TE2PA^{2-} [43] and PYTA^{4-} [39] were synthesized according to previously reported procedures. The Dy(III) complexes [Dy(PYTA)]$^-$ and [Dy(NO3PA)] were prepared by mixing equimolar amounts of ligand and $Dy(NO_3)_3\cdot6H_2O$ in either D_2O or H_2O, and adjustment of the pH to ~7.0 using a diluted NaOH solution. [Dy(CB-TE2PA)]$^+$ was prepared in a microwave apparatus, following the procedure reported for the Eu(III) complex,[43] and the resulting complex was then redissolved in either H_2O or D_2O. NMR measurements were recorded using complex concentrations of ~30 mM. ^{1}H NMR spectra were recorded in Bruker DPX 250 (5.87 T), Bruker Avance 300 (7.05 T), Bruker ARX400 (9.40 T) and Bruker Avance 500 (11.75 T) spectrometers. Linewidths were measured with the deconvolution tool of MestRe Nova,[92] using Lorentzian functions (Figure S13, Supporting Information). Single crystals of $[Dy(CB\text{-}TE2PA)](PF_6)\cdot2.5H_2O$ were obtained by slow evaporation of an aqueous solution of the complex in the presence of excess KPF_6.

Luminescence measurements. Spectroscopic measurements were performed with 10×10 mm² quartz suprasil certified cells (Helma Analytics). UV/Vis absorption spectra were recorded on a lambda 950 UV/VIS/NIR absorption spectrometer from Perkin Elmer. Steady-state emission spectra were recorded on an Edinburgh Instruments FLP920 working with a continuous 450 W Xe lamp and a red sensitive R928 photomultiplier from Hamamatsu in Pelletier housing for visible detection (230 to 900 nm) or a Hamamatsu R5 509-72 photomultiplier cooled at 77 K for the Vis-NIR part. A 330 nm high pass cut-off filter was used to eliminate the second order artefacts for the visible part and a 850 nm high pass cut-off filter for the NIR part. Luminescence lifetimes were measured on the same instrument working in the Multi Channels Spectroscopy mode and using a Xenon flash lamp as the excitation source. The decay curves were corrected for intensity profile of the lamp by measuring the diffraction signals of a scattering sample of colloidal silica. Errors on the luminescence lifetimes are estimated to ±10%. Luminescence quantum yields were measured according to conventional procedures, with diluted solutions (optical density < 0.05 at the excitation wavelength), using Rhodamine 6G in water (φ = 76%).[67] High resolution emission spectra were recorded at 77K using a nitrogen cooled oxford instrument cryostat with 0.05 nm slits at the emission, except for [Dy(CB-TE2PA)]$^+$ for which slits of 0.1 nm were used due to the weaker intensity.

X-ray diffraction measurements. A crystal of $[Dy(CB\text{-}TE2PA)](PF_6)\cdot2.5H_2O$ was analysed by X-ray diffraction. Crystallographic data and structure refinement parameters are shown in Table S2 (Supporting Information). Crystallographic data were collected on a Bruker D8 Venture diffractometer with a Photon 100 CMOS detector at 100 K with Mo-Kα radiation (λ = 0.71073 Å) generated by an Incoatec high brillance microfocus source equipped with Incoatec Helios multilayer optics. The APEX3[93] software was used for collecting frames of data, indexing reflections, and the determination of lattice parameters, while SAINT[94] was used for integration of intensity of reflections, and SADABS[95] for scaling and empirical absorption correction. The structure was solved by dual-space methods using the program SHELXT.[96] All non-hydrogen atoms were refined with anisotropic thermal parameters by full-matrix least-squares calculations on F^2 using the program SHELXL-2014.[97] Hydrogen atoms of the compound were inserted at calculated positions and constrained with isotropic thermal parameters. CCDC 2257994 contains the supplementary crystallographic data, which can be obtained free of charge from the Cambridge Crystallographic Data Centre via www.ccdc.ac.uk/data_request/cif.

Computational details. The geometries of the Dy(III) complexes were optimized using Gaussian 16,[98] employing the hybrid-meta GGA functional TPSSh,[99] in combination with the small-core quasi-relativistic effective core potential proposed by Dolg et al.[100] (28 electrons, 1s-3d, in the core for Dy) and the associated ECP28MWB_GUESS basis set, which possesses a (42s26p20d8f)/[3s2p2d1f] contraction scheme. The standard Def2-TZVPP basis set was used for the ligand atoms.[101] Solvent effects were incorporated using the polarized continuum model (IEF-PCM variant).[102,103] Frequency calculations were employed to confirm that the optimized geometries corresponded to true energy minima.

Complete active space self-consistent field (CASSCF)[104] calculations were carried out using the ORCA program package (version 5.0.3).[105,106] The active space included the nine electrons of Dy(III) distributed over the seven 4f orbitals [CASSCF(9,7)]. The state average CASSCF calculation included 21 sextet, 224 quartet and 490 doublet roots. In these calculations we used the SARC2-DKH-QZVP[107] basis set for Dy and its associated SARC2-DKH-QZVP/JK auxiliary basis set to accelerate the calculations with the resolution of identity and chain of spheres (RIJCOSX)[108,109] method. For ligand atoms we used the DKH-def2-TZVPP[101] basis set and auxiliary basis sets generated by ORCA with the Autoaux[110] procedure. Relativistic effects were taken into account with the Douglas –Kroll-Hess (DKH2) method,[111,112] using a finite nucleus model.[113] SOC effects were incorporated using quasi-degenerate perturbation theory (QDPT).[114,115] Solvent effects were included using the SMD solvation model.[116]

ASSOCIATED CONTENT

Absorption and emission spectra, additional NMR data and computational data. This material is available free of charge via the Internet at http://pubs.acs.org.

AUTHOR INFORMATION

Corresponding Authors

Carlos Platas-Iglesias - *Universidade da Coruña, Centro Interdisciplinar de Química e Bioloxía (CICA) and Departamento de Química, Facultade de Ciencias, 15071, A Coruña, Galicia, Spain*; orcid.org/0000-0002-6989-9654;
Email: carlos.platas.iglesias@udc.es

Authors

Charlene Harriswangler - *Universidade da Coruña, Centro Interdisciplinar de Química e Bioloxía (CICA) and Departamento de Química, Facultade de Ciencias, 15071, A Coruña, Galicia, Spain*.

Fátima Lucio-Martínez - *Universidade da Coruña, Centro Interdisciplinar de Química e Bioloxía (CICA) and Departamento de Química, Facultade de Ciencias, 15071, A Coruña, Galicia, Spain;*

Léna Godec - *Equipe de Synthèse Pour l'Analyse (SynPA), Institut Pluridisciplinaire Hubert Curien (IPHC), UMR 7178, CNRS, Université de Strasbourg, ECPM, 25 rue Becquerel, 67087, Strasbourg Cedex, France.*

Kevin Lohona Soro - *Equipe de Synthèse Pour l'Analyse (SynPA), Institut Pluridisciplinaire Hubert Curien (IPHC), UMR 7178, CNRS, Université de Strasbourg, ECPM, 25 rue Becquerel, 67087, Strasbourg Cedex, France.*

Laura Valencia - *Departamento de Química Inorgánica, Facultade de Ciencias, Universidade de Vigo, As Lagoas, Marcosende, 36310 Pontevedra, Spain.*

Aurora Rodríguez-Rodríguez – *Universidade da Coruña, Centro Interdisciplinar de Química e Bioloxía (CICA) and Departamento de Química, Facultade de Ciencias, 15071, A Coruña, Galicia, Spain*;

David Esteban-Gómez – *Universidade da Coruña, Centro Interdisciplinar de Química e Bioloxía (CICA) and Departamento de Química, Facultade de Ciencias, 15071, A Coruña, Galicia, Spain*;

Loïc Charbonnière - - *Equipe de Synthèse Pour l'Analyse (SynPA), Institut Pluridisciplinaire Hubert Curien (IPHC), UMR 7178, CNRS, Université de Strasbourg, ECPM, 25 rue Becquerel, 67087, Strasbourg Cedex, France*

Author Contributions

The manuscript was written through contributions of all authors. All authors have given approval to the final version of the manuscript.

Notes

The authors declare no competing financial interest.

ACKNOWLEDGMENTS

This research was funded by the Spanish Ministry for Science and Innovation, the National Research Agency and FEDER funds from the EU (grants PID2019-104626GB-I00), Xunta de Galicia (Grants ED431B 2017/59 and ED431D 2017/01). C.-H. thanks Ministerio Ciencia e Innovación (Grant PRE2020-092888) for funding her PhD contract. The authors also thank Centro de Supercomputación de Galicia (CESGA) for providing the supercomputing facilities. L.J.C. and L.G. thanks the French national research agency for financial support (ANR LUCAS, n° ANR-19-CE29-0014-01).

REFERENCES

(1) Piguet, C. Set Aside When Building the Periodic Table 150 Years Ago, Are Rare Earths Any Better Considered by Chemists in the 21st Century? *CHIMIA* **2019**, *73* (3), 165. https://doi.org/10.2533/chimia.2019.165.

(2) Peters, J. A.; Djanashvili, K.; Geraldes, C. F. G. C.; Platas-Iglesias, C. The Chemical Consequences of the Gradual Decrease of the Ionic Radius along the Ln-Series. *Coord. Chem. Rev.* **2020**, *406*, 213146. https://doi.org/10.1016/j.ccr.2019.213146.

(3) Bünzli, J.-C. G.; Piguet, C. Lanthanide-Containing Molecular and Supramolecular Polymetallic Functional Assemblies. *Chem. Rev.* **2002**, *102* (6), 1897–1928. https://doi.org/10.1021/cr010299j.

(4) Seitz, M.; Oliver, A. G.; Raymond, K. N. The Lanthanide Contraction Revisited. *J. Am. Chem. Soc.* **2007**, *129* (36), 11153–11160. https://doi.org/10.1021/ja072750f.

(5) Shannon, R. D. Revised Effective Ionic Radii and Systematic Studies of Interatomic Distances in Halides and Chaleogenides. *Acta Crystallogr. A 32*, 751–767.

(6) Cotton, S. A. Establishing Coordination Numbers for the Lanthanides in Simple Complexes. *Comptes Rendus Chim.* **2005**, *8* (2), 129–145. https://doi.org/10.1016/j.crci.2004.07.002.

(7) Friedman, H. G.; Choppin, G. R.; Feuerbacher, D. G. The Shapes of the f Orbitals. *J. Chem. Educ.* **1964**, *41* (7), 354. https://doi.org/10.1021/ed041p354.

(8) Alsaadi, B. M.; Rossotti, F. J. C.; Williams, R. J. P. Electron Relaxation Rates of Lanthanide Aquo-Cations. *J. Chem. Soc. Dalton Trans.* **1980**, No. 11, 2147. https://doi.org/10.1039/dt9800002147.

(9) Cockerill, A. F.; Davies, G. L. O.; Harden, R. C.; Rackham, D. M. Lanthanide Shift Reagents for Nuclear Magnetic Resonance Spectroscopy. *Chem. Rev.* **1973**, *73* (6), 553–588. https://doi.org/10.1021/cr60286a001.

(10) Bertini, I.; Luchinat, C.; Parigi, G. Magnetic Susceptibility in Paramagnetic NMR. *Prog. Nucl. Magn. Reson. Spectrosc.* **2002**, *40*, 249–273. https://doi.org/10.1002/CHIN.200301277.

(11) Bertini, I.; Janik, M. B. L.; Lee, Y.-M.; Luchinat, C.; Rosato, A. Magnetic Susceptibility Tensor Anisotropies for a Lanthanide Ion Series in a Fixed Protein Matrix. *J. Am. Chem. Soc.* **2001**, *123* (18), 4181–4188. https://doi.org/10.1021/ja0028626.

(12) Di Pietro, S.; Piano, S. L.; Di Bari, L. Pseudocontact Shifts in Lanthanide Complexes with Variable Crystal Field Parameters. *Coord. Chem. Rev.* **2011**, *255* (23–24), 2810–2820. https://doi.org/10.1016/j.ccr.2011.05.010.

(13) Viswanathan, S.; Kovacs, Z.; Green, K. N.; Ratnakar, S. J.; Sherry, A. D. Alternatives to Gadolinium-Based Metal Chelates for Magnetic Resonance Imaging. *Chem. Rev.* **2010**, *110* (5), 2960–3018. https://doi.org/10.1021/cr900284a.

(14) Evbuomwan, O. M.; Terreno, E.; Aime, S.; Sherry, A. D. CEST and PARACEST Agents for Molecular Imaging. In *The Chemistry of Molecular Imaging*; Long, N., Wong, W.-T., Eds.; John Wiley & Sons, Inc: Hoboken, NJ, 2014; pp 225–243. https://doi.org/10.1002/9781118854754.ch10.

(15) Woods, M.; Woessner, D. E.; Sherry, A. D. Paramagnetic Lanthanide Complexes as PARACEST Agents for Medical Imaging. *Chem. Soc. Rev.* **2006**, *35* (6), 500. https://doi.org/10.1039/b509907m.

(16) Zhang, S.; Merritt, M.; Woessner, D. E.; Lenkinski, R. E.; Sherry, A. D. PARACEST Agents: Modulating MRI Contrast via Water Proton Exchange. *Acc. Chem. Res.* **2003**, *36* (10), 783–790. https://doi.org/10.1021/ar020228m.

(17) Tóth, É.; Bonnet, C. S. Responsive ParaCEST Contrast Agents. *Inorganics* **2019**, *7* (5), 68. https://doi.org/10.3390/inorganics7050068.

(18) Finney, K.-L. N. A.; Harnden, A. C.; Rogers, N. J.; Senanayake, P. K.; Blamire, A. M.; O'Hogain, D.; Parker, D. Simultaneous Triple Imaging with Two PARASHIFT Probes: Encoding Anatomical, PH and Temperature Information Using Magnetic Resonance Shift Imaging. *Chem. - Eur. J.* **2017**, *23* (33), 7976–7989. https://doi.org/10.1002/chem.201700447.

(19) Harvey, P.; Blamire, A. M.; Wilson, J. I.; Finney, K.-L. N. A.; Funk, A. M.; Senanayake, P. K.; Parker, D. Moving the Goal Posts: Enhancing the Sensitivity of PARASHIFT Proton Magnetic Resonance Imaging and Spectroscopy. *Chem. Sci.* **2013**, *4* (11), 4251. https://doi.org/10.1039/c3sc51526e.

(20) Mason, K.; Rogers, N. J.; Suturina, E. A.; Kuprov, I.; Aguilar, J. A.; Batsanov, A. S.; Yufit, D. S.; Parker, D. PARASHIFT Probes: Solution NMR and X-Ray Structural Studies of Macrocyclic Ytterbium and Yttrium Complexes. *Inorg. Chem.* **2017**, *56* (7), 4028–4038. https://doi.org/10.1021/acs.inorgchem.6b02291.

(21) Rodríguez-Rodríguez, A.; Zaiss, M.; Esteban-Gómez, D.; Angelovski, G.; Platas-Iglesias, C. Paramagnetic Chemical Exchange Saturation Transfer Agents and Their Perspectives for Application in Magnetic Resonance Imaging. *Int. Rev. Phys. Chem.* **2021**, *40* (1), 51–79. https://doi.org/10.1080/0144235X.2020.1823167.

(22) Peters, J. A.; Huskens, J.; Raber, D. J. Lanthanide Induced Shifts and Relaxation Rate Enhancements. *Prog. Nucl. Magn. Reson. Spectrosc.* **1996**, *28* (3–4), 283–350. https://doi.org/10.1016/0079-6565(95)01026-2.

(23) Vipond, J.; Woods, M.; Zhao, P.; Tircso, G.; Ren, J.; Bott, S. G.; Ogrin, D.; Kiefer, G. E.; Kovacs, Z.; Sherry, A. D. A Bridge to Coordination Isomer Selection in Lanthanide(III) DOTA-Tetraamide Complexes. **2007**, *46*, 2584−2595. https://doi.org/10.1021/ic062184+.

(24) Di Bari, L.; Salvadori, P. Solution Structure of Chiral Lanthanide Complexes. *Coord. Chem. Rev.* **2005**, *249* (24), 2854–2879. https://doi.org/10.1016/j.ccr.2005.03.006.

(25) Berardozzi, R.; Di Bari, L. A Simple and General Method to Determine Reliable Pseudocontact Shifts in Lanthanide Complexes. *Inorg. Chem.* **2013**, *52* (19), 11514–11518. https://doi.org/10.1021/ic401825f.

(26) Doffek, C.; Alzakhem, N.; Bischof, C.; Wahsner, J.; Güden-Silber, T.; Lügger, J.; Platas-Iglesias, C.; Seitz, M. Understanding the Quenching Effects of Aromatic C–H- and C–D-Oscillators in Near-IR Lanthanoid Luminescence. *J. Am. Chem. Soc.* **2012**, *134* (39), 16413–16423. https://doi.org/10.1021/ja307339f.

(27) Parigi, G.; Ravera, E.; Luchinat, C. Magnetic Susceptibility and Paramagnetism-Based NMR. *Prog. Nucl. Magn. Reson. Spectrosc.* **2019**, *114–115*, 211–236. https://doi.org/10.1016/j.pnmrs.2019.06.003.

(28) Funk, A. M.; Finney, K.-L. N. A.; Harvey, P.; Kenwright, A. M.; Neil, E. R.; Rogers, N. J.; Kanthi Senanayake, P.; Parker, D. Critical Analysis of the Limitations of Bleaney's Theory of Magnetic Anisotropy in Paramagnetic Lanthanide Coordination Complexes. *Chem. Sci.* **2015**, *6* (3), 1655–1662. https://doi.org/10.1039/C4SC03429E.

(29) Suturina, E. A.; Mason, K.; Geraldes, C. F. G. C.; Kuprov, I.; Parker, D. Beyond Bleaney's Theory: Experimental and Theoretical Analysis of Periodic Trends in Lanthanide-Induced Chemical Shift. *Angew. Chem.* **2017**, *129* (40), 12383–12386. https://doi.org/10.1002/ange.201706931.

(30) Castro, G.; Regueiro-Figueroa, M.; Esteban-Gómez, D.; Pérez-Lourido, P.; Platas-Iglesias, C.; Valencia, L. Magnetic Anisotropies in Rhombic Lanthanide(III) Complexes Do Not Conform to Bleaney's Theory. *Inorg. Chem.* **2016**, *55* (7), 3490–3497. https://doi.org/10.1021/acs.inorgchem.5b02918.

(31) Bleaney, B. Nuclear Magnetic Resonance Shifts in Solution Due to Lanthanide Ions. *J. Magn. Reson. 1969* **1972**, *8* (1), 91–100. https://doi.org/10.1016/0022-2364(72)90027-3.

(32) Suturina, E. A.; Mason, K.; Botta, M.; Carniato, F.; Kuprov, I.; Chilton, N. F.; McInnes, E. J. L.; Vonci, M.; Parker, D. Periodic Trends and Hidden Dynamics of Magnetic Properties in Three Series of Triazacyclononane Lanthanide Complexes. *Dalton Trans.* **2019**, *48* (23), 8400–8409. https://doi.org/10.1039/C9DT01069F.

(33) Solomon, I. Relaxation Processes in a System of Two Spins. *Phys. Rev.* **1955**, *99*, 559–565. https://doi.org/10.1103/PhysRev.99.559.

(34) Bloembergen, N. Proton Relaxation Times in Paramagnetic Solutions. *J. Chem. Phys.* **1957**, *27* (2), 572–573. https://doi.org/10.1063/1.1743771.

(35) Bloembergen, N.; Morgan, L. O. Proton Relaxation Times in Paramagnetic Solutions. Effects of Electron Spin Relaxation. *J. Chem. Phys.* **1961**, *34* (3), 842–850. https://doi.org/10.1063/1.1731684.

(36) Funk, A. M.; Harvey, P.; Finney, K.-L. N. A.; Fox, M. A.; Kenwright, A. M.; Rogers, N. J.; Senanayake, P. K.; Parker, D. Challenging Lanthanide Relaxation Theory: Erbium and Thulium Complexes That Show NMR Relaxation Rates Faster than Dysprosium and Terbium Analogues. *Phys. Chem. Chem. Phys.* **2015**, *17* (25), 16507–16511. https://doi.org/10.1039/C5CP02210J.

(37) Piguet, C.; Geraldes, C. F. G. C. Paramagnetic NMR Lanthanide Induced Shifts for Extracting Solution Structures. In *Handbook on the Physics and Chemistry of Rare Earths*; Elsevier, 2003; Vol. 33, pp 353–463. https://doi.org/10.1016/S0168-1273(02)33005-8.

(38) Aime, S.; Barbero, L.; Botta, M.; Ermondi, G. Determination of MetaI-Proton Distances and Electronic Relaxation Times in Lanthanide Complexes by Nuclear Magnetic Resonance Spectroscopy. *J Chem Soc Dalton Trans* **1992**, 225–228.

(39) Valencia, L.; Martinez, J.; Macías, A.; Bastida, R.; Carvalho, R. A.; Geraldes, C. F. G. C. X-Ray Diffraction and ^{1}H NMR in Solution: Structural Determination of Lanthanide Complexes of a $Py_2N_6Ac_4$ Ligand. *Inorg. Chem.* **2002**, *41* (20), 5300–5312. https://doi.org/10.1021/ic0257017.

(40) Nocton, G.; Nonat, A.; Gateau, C.; Mazzanti, M. Water Stability and Luminescence of Lanthanide Complexes of Tripodal Ligands Derived from 1,4,7-Triazacyclononane: Pyridinecarboxamide *versus* Pyridinecarboxylate Donors. *Helv. Chim. Acta* **2009**, *92* (11), 2257–2273. https://doi.org/10.1002/hlca.200900150.

(41) Gateau, C.; Mazzanti, M.; Pécaut, J.; Dunand, F. A.; Helm, L. Solid-State and Solution Properties of the Lanthanide Complexes of a New Nonadentate Tripodal Ligand Derived from 1,4,7-Triazacyclononane. *Dalton Trans* **2003**, No. 12, 2428–2433. https://doi.org/10.1039/B303079B.

(42) Walton, J. W.; Carr, R.; Evans, N. H.; Funk, A. M.; Kenwright, A. M.; Parker, D.; Yufit, D. S.; Botta, M.; De Pinto, S.; Wong, K.-L. Isostructural Series of Nine-Coordinate Chiral Lanthanide Complexes Based on Triazacyclononane. *Inorg. Chem.* **2012**, *51* (15), 8042–8056. https://doi.org/10.1021/ic300147p.

(43) Rodríguez-Rodríguez, A.; Esteban-Gómez, D.; Tripier, R.; Tircsó, G.; Garda, Z.; Tóth, I.; de Blas, A.; Rodríguez-Blas, T.; Platas-Iglesias, C. Lanthanide(III) Complexes with a Reinforced Cyclam Ligand Show Unprecedented Kinetic Inertness. *J. Am. Chem. Soc.* **2014**, *136* (52), 17954–17957. https://doi.org/10.1021/ja511331n.

(44) Rodríguez-Rodríguez, A.; Regueiro-Figueroa, M.; Esteban-Gómez, D.; Tripier, R.; Tircsó, G.; Kálmán, F. K.; Bényei, A. C.; Tóth, I.; Blas, A. de; Rodríguez-Blas, T.; Platas-Iglesias, C. Complexation of Ln^{3+} Ions with Cyclam Dipicolinates: A Small Bridge That Makes Huge Differences in Structure, Equilibrium, and Kinetic Properties. *Inorg. Chem.* **2016**, *55* (5), 2227–2239. https://doi.org/10.1021/acs.inorgchem.5b02627.

(45) Woods, M.; Payne, K. M.; Valente, E. J.; Kucera, B. E.; Young, V. G. Crystal Structures of DOTMA Chelates from Ce^{3+} to Yb^{3+} : Evidence for a Continuum of Metal Ion Hydration States. *Chem. – Eur. J.* **2019**, *25* (42), 9997–10005. https://doi.org/10.1002/chem.201902068.

(46) Polášek, M.; Rudovský, J.; Hermann, P.; Lukeš, I.; Elst, L. V.; Muller, R. N. Lanthanide(III) Complexes of a Pyridine N-Oxide Analogue of DOTA: Exclusive M Isomer Formation Induced by a Six-Membered Chelate Ring. *Chem Commun* **2004**, No. 22, 2602–2603. https://doi.org/10.1039/B409996F.

(47) Santria, A.; Fuyuhiro, A.; Fukuda, T.; Ishikawa, N. Synthesis of a Series of Heavy Lanthanide(III) Monoporphyrinato Complexes with Tetragonal Symmetry. *Inorg. Chem.* **2017**, *56* (17), 10625–10632. https://doi.org/10.1021/acs.inorgchem.7b01546.

(48) Dale, J. Exploratory Calculations of Medium and Large Rings. *Acta Chem. Scand.* **1973**, *27*, 1115–1129. https://doi.org/10.3891/acta.chem.scand.27-1115.

(49) Grenier, L.; Beyler, M.; Platas- Iglesias, C.; Closson, T.; Gómez, D. E.; Seferos, D. S.; Liu, P.; Ornatsky, O. I.; Baranov, V.; Tripier, R. Highly Stable and Inert Complexation of Indium(III) by Reinforced Cyclam Dipicolinate and a Bifunctional Derivative for Bead Encoding in Mass Cytometry. *Chem. – Eur. J.* **2019**, *25* (67), 15387–15400. https://doi.org/10.1002/chem.201903969.

(50) Wong, E. H.; Weisman, G. R.; Hill, D. C.; Reed, D. P.; Rogers, M. E.; Condon, J. S.; Fagan, M. A.; Calabrese, J. C.; Lam, K.-C.; Guzei, I. A.; Rheingold, A. L. Synthesis and Characterization of Cross-Bridged Cyclams and Pendant-Armed Derivatives and Structural Studies of Their Copper(II) Complexes. *J. Am. Chem. Soc.* **2000**, *122* (43), 10561–10572. https://doi.org/10.1021/ja001295j.

(51) Pujales-Paradela, R.; Savić, T.; Brandariz, I.; Pérez-Lourido, P.; Angelovski, G.; Esteban-Gómez, D.; Platas-Iglesias, C. Reinforced Ni(II)-Cyclam Derivatives as Dual $^{1}H/^{19}F$ MRI Probes. *Chem. Commun.* **2019**, *55* (28), 4115–4118. https://doi.org/10.1039/C9CC01204D.

(52) Nonat, A.; Gateau, C.; Fries, P. H.; Mazzanti, M. Lanthanide Complexes of a Picolinate Ligand Derived from 1,4,7-Triazacyclononane with Potential Application in Magnetic Resonance Imaging and Time-Resolved Luminescence Imaging. *Chem Eur J* **2006**, *12*, 7133–7150.

(53) Sy, M.; Esteban- Gómez, D.; Platas- Iglesias, C.; Rodríguez- Rodríguez, A.; Tripier, R.; Charbonnière, L. J. Spectroscopic Properties of a Family of Mono- to Trinuclear Lanthanide Complexes. *Eur. J. Inorg. Chem.* **2017**, *2017* (14), 2122–2129. https://doi.org/10.1002/ejic.201601516.

(54) Xiong, J.; Yang, Z.-X.; Ma, P.; Lin, D.; Zheng, Q.; Huo, Y. PH-Controlled Assembly of Two Polynuclear Dy(III)-Containing Polytungstoarsenates with Magnetic and Luminescence Properties. *Inorg. Chem.* **2021**, *60* (10), 7519–7526. https://doi.org/10.1021/acs.inorgchem.1c00859.

(55) Galaup, C.; Couchet, J. M.; Picard, C.; Tisnès, P. Novel Terpyridine Macrocyclic Complexing Agent and Luminescence of Its Neutral Ln(III) Complexes (Ln=Eu, Tb, Sm, Dy) in Aqueous Solution. *Tetrahedron Lett.* **2001**, *42* (36), 6275–6278. https://doi.org/10.1016/S0040-4039(01)01243-6.

(56) Wei, C.; Sun, B.; Zhao, Z.; Cai, Z.; Liu, J.; Tan, Y.; Wei, H.; Liu, Z.; Bian, Z.; Huang, C. A Family of Highly Emissive Lanthanide Complexes Constructed with 6-(Diphenylphosphoryl)Picolinate. *Inorg. Chem.* **2020**, *59* (13), 8800–8808. https://doi.org/10.1021/acs.inorgchem.0c00444.

(57) Biju, S.; Gopakumar, N.; Bünzli, J.-C. G.; Scopelliti, R.; Kim, H. K.; Reddy, M. L. P. Brilliant Photoluminescence and Triboluminescence from Ternary Complexes of Dy^{III} and Tb^{III} with 3-Phenyl-4-Propanoyl-5-Isoxazolonate and a Bidentate Phosphine Oxide Coligand. *Inorg. Chem.* **2013**, *52* (15), 8750–8758. https://doi.org/10.1021/ic400913f.

(58) Kofod, N.; Arppe-Tabbara, R.; Sørensen, T. J. Electronic Energy Levels of Dysprosium(III) Ions in Solution. Assigning the Emitting State and the Intraconfigurational 4f–4f Transitions in the Vis–NIR Region and Photophysical Characterization of Dy(III) in Water, Methanol, and Dimethyl Sulfoxide. *J. Phys. Chem. A* **2019**, *123* (13), 2734–2744. https://doi.org/10.1021/acs.jpca.8b12034.

(59) Law, G.-L.; Pham, T. A.; Xu, J.; Raymond, K. N. A Single Sensitizer for the Excitation of Visible and NIR Lanthanide Emitters in Water with High Quantum Yields. *Angew. Chem. Int. Ed.* **2012**, *51* (10), 2371–2374. https://doi.org/10.1002/anie.201106748.

(60) Brunet, E.; Juanes, O.; Sedano, R.; Rodríguez-Ubis, J.-C. Lanthanide Complexes of Polycarboxylate-Bearing Dipyrazolylpyridine Ligands with near-Unity Luminescence Quantum Yields: The Effect of Pyridine Substitution. *Photochem. Photobiol. Sci.* **2002**, *1* (8), 613–618. https://doi.org/10.1039/b204544c.

(61) Bui, A. T.; Roux, A.; Grichine, A.; Duperray, A.; Andraud, C.; Maury, O. Twisted Charge-Transfer Antennae for Ultra-Bright Terbium(III) and Dysprosium(III) Bioprobes. *Chem. - Eur. J.* **2018**, *24* (14), 3408–3412. https://doi.org/10.1002/chem.201705933.

(62) Petoud, S.; Muller, G.; Moore, E. G.; Xu, J.; Sokolnicki, J.; Riehl, J. P.; Le, U. N.; Cohen, S. M.; Raymond, K. N. Brilliant Sm, Eu, Tb, and Dy Chiral Lanthanide Complexes with Strong Circularly Polarized Luminescence. *J. Am. Chem. Soc.* **2007**, *129* (1), 77–83. https://doi.org/10.1021/ja064902x.

(63) Hamon, N.; Roux, A.; Beyler, M.; Mulatier, J.-C.; Andraud, C.; Nguyen, C.; Maynadier, M.; Bettache, N.; Duperray, A.; Grichine, A.; Brasselet, S.; Gary-Bobo, M.;

Maury, O.; Tripier, R. Pyclen-Based Ln(III) Complexes as Highly Luminescent Bioprobes for *In Vitro* and *In Vivo* One- and Two-Photon Bioimaging Applications. *J. Am. Chem. Soc.* **2020**, *142* (22), 10184–10197. https://doi.org/10.1021/jacs.0c03496.

(64) Kimura, T.; Kato, Y. Luminescence Study on Determination of the Hydration Number of Sm(III) and Dy(III). *J. Alloys Compd.* **1995**, *225* (1–2), 284–287. https://doi.org/10.1016/0925-8388(94)07084-9.

(65) Petoud, S.; Cohen, S. M.; Bünzli, J.-C. G.; Raymond, K. N. Stable Lanthanide Luminescence Agents Highly Emissive in Aqueous Solution: Multidentate 2-Hydroxyisophthalamide Complexes of Sm^{3+}, Eu^{3+}, Tb^{3+}, Dy^{3+}. *J. Am. Chem. Soc.* **2003**, *125* (44), 13324–13325. https://doi.org/10.1021/ja0379363.

(66) Wartenberg, N.; Raccurt, O.; Bourgeat- Lami, E.; Imbert, D.; Mazzanti, M. Multicolour Optical Coding from a Series of Luminescent Lanthanide Complexes with a Unique Antenna. *Chem. – Eur. J.* **2013**, *19* (10), 3477–3482. https://doi.org/10.1002/chem.201203657.

(67) Olmsted, John. Calorimetric Determinations of Absolute Fluorescence Quantum Yields. *J. Phys. Chem.* **1979**, *83* (20), 2581–2584. https://doi.org/10.1021/j100483a006.

(68) Vonci, M.; Mason, K.; Suturina, E. A.; Frawley, A. T.; Worswick, S. G.; Kuprov, I.; Parker, D.; McInnes, E. J. L.; Chilton, N. F. Rationalization of Anomalous Pseudocontact Shifts and Their Solvent Dependence in a Series of C_3-Symmetric Lanthanide Complexes. *J. Am. Chem. Soc.* **2017**, *139* (40), 14166–14172. https://doi.org/10.1021/jacs.7b07094.

(69) Guettas, D.; Gendron, F.; Fernandez Garcia, G.; Riobé, F.; Roisnel, T.; Maury, O.; Pilet, G.; Cador, O.; Guennic, B. L. Luminescence-Driven Electronic Structure Determination Ina Textbook Dimeric Dy^{III}-Based Single-Molecule Magnet. *Chem. - Eur. J.* **2020**, *26*, 4389–4395. https://doi.org/doi.org/10.1002/chem.201905493.

(70) Esteban-Gómez, D.; Büldt, L. A.; Pérez-Lourido, P.; Valencia, L.; Seitz, M.; Platas-Iglesias, C. Understanding the Optical and Magnetic Properties of Ytterbium(III) Complexes. *Inorg. Chem.* **2019**, *58* (6), 3732–3743. https://doi.org/10.1021/acs.inorgchem.8b03354.

(71) Cucinotta, G.; Perfetti, M.; Luzon, J.; Etienne, M.; Car, P.-E.; Caneschi, A.; Calvez, G.; Bernot, K.; Sessoli, R. Magnetic Anisotropy in a Dysprosium/DOTA Single-Molecule Magnet: Beyond Simple Magneto-Structural Correlations. *Angew. Chem. Int. Ed.* **2012**, *51* (7), 1606–1610. https://doi.org/10.1002/anie.201107453.

(72) Lukeš, I.; Kotek, J.; Vojtíšek, P.; Hermann, P. Complexes of Tetraazacycles Bearing Methylphosphinic/Phosphonic Acid Pendant Arms with Copper(II), Zinc(II) and Lanthanides(III). A Comparison with Their Acetic Acid Analogues. *Coord. Chem. Rev.* **2001**, *216–217*, 287–312. https://doi.org/10.1016/S0010-8545(01)00336-8.

(73) Blackburn, O. A.; Chilton, N. F.; Keller, K.; Tait, C. E.; Myers, W. K.; McInnes, E. J. L.; Kenwright, A. M.; Beer, P. D.; Timmel, C. R.; Faulkner, S. Spectroscopic and Crystal Field Consequences of Fluoride Binding by $[Yb{\cdot}DTMA]^{3+}$ in Aqueous Solution. *Angew. Chem. Int. Ed.* **2015**, *54* (37), 10783–10786. https://doi.org/10.1002/anie.201503421.

(74) Pinkerton, A. A.; Rossier, M.; Spiliadis, S. Lanthanide-Induced Contact Shifts. the Average Electron Spin Polarization, Theory and Experiment. *J. Magn. Reson. 1969* **1985**, *64* (3), 420–425. https://doi.org/10.1016/0022-2364(85)90104-0.

(75) Lisowski, J.; Sessler, J. L.; Lynch, V.; Mody, T. D. ^{1}H NMR Spectroscopic Study of Paramagnetic Lanthanide(III) Texaphyrins. Effect of Axial Ligation. *J. Am. Chem. Soc.* **1995**, *117*, 2273–2285. https://doi.org/10.1021/ja00113a016.

(76) Rodríguez-Rodríguez, A.; Esteban-Gómez, D.; de Blas, A.; Rodríguez-Blas, T.; Botta, M.; Tripier, R.; Platas-Iglesias, C. Solution Structure of Ln(III) Complexes with Macrocyclic Ligands Through Theoretical Evaluation of ^{1}H NMR Contact Shifts. *Inorg. Chem.* **2012**, *51* (24), 13419–13429. https://doi.org/10.1021/ic302322r.

(77) Castro, G.; Wang, G.; Gambino, T.; Esteban-Gómez, D.; Valencia, L.; Angelovski, G.; Platas-Iglesias, C.; Pérez-Lourido, P. Lanthanide(III) Complexes Based on an 18-Membered Macrocycle Containing Acetamide Pendants. Structural Characterization and ParaCEST Properties. *Inorg. Chem.* **2021**, *60* (3), 1902–1914. https://doi.org/10.1021/acs.inorgchem.0c03385.

(78) Willcott, M. R.; Lenkinski, R. E.; Davis, R. E. Interpretation of the Pseudocontact Model for Nuclear Magnetic Resonance Shift Reagents. I. Agreement Factor, R. *J. Am. Chem. Soc.* **1972**, *94* (5), 1742–1744. https://doi.org/10.1021/ja00760a054.

(79) Strickland, M.; Schwieters, C. D.; Göbl, C.; Opina, A. C. L.; Strub, M.-P.; Swenson, R. E.; Vasalatiy, O.; Tjandra, N. Characterizing the Magnetic Susceptibility Tensor of Lanthanide-Containing Polymethylated-DOTA Complexes. *J. Biomol. NMR* **2016**, *66* (2), 125–139. https://doi.org/10.1007/s10858-016-0061-x.

(80) Keizers, P. H. J.; Saragliadis, A.; Hiruma, Y.; Overhand, M.; Ubbink, M. Design, Synthesis, and Evaluation of a Lanthanide Chelating Protein Probe: CLaNP-5 Yields Predictable Paramagnetic Effects Independent of Environment. *J. Am. Chem. Soc.* **2008**, *130* (44), 14802–14812. https://doi.org/10.1021/ja8054832.

(81) Vega, A. J.; Fiat, D. Nuclear Relaxation Processes of Paramagnetic Complexes The Slow-Motion Case. *Mol. Phys.* **1976**, *31* (2), 347–355. https://doi.org/10.1080/00268977600100261.

(82) Dunand, F. A.; Borel, A.; Merbach, A. E. How Does Internal Motion Influence the Relaxation of the Water Protons in Ln^{III} DOTA-like Complexes? *J. Am. Chem. Soc.* **2002**, *124* (4), 710–716. https://doi.org/10.1021/ja016873q.

(83) Pujales-Paradela, R.; Savić, T.; Pérez-Lourido, P.; Esteban-Gómez, D.; Angelovski, G.; Botta, M.; Platas-Iglesias, C. Lanthanide Complexes with ^{1}H ParaCEST and ^{19}F Response for Magnetic Resonance Imaging Applications. *Inorg. Chem.* **2019**, *58* (11), 7571–7583. https://doi.org/10.1021/acs.inorgchem.9b00869.

(84) Suturina, E. A.; Mason, K.; Geraldes, C. F. G. C.; Chilton, N. F.; Parker, D.; Kuprov, I. Lanthanide-Induced Relaxation Anisotropy. *Phys. Chem. Chem. Phys.* **2018**, *20* (26), 17676–17686. https://doi.org/10.1039/C8CP01332B.

(85) Powell, D. H.; Dhubhghaill, O. M. N.; Pubanz, D.; Helm, L.; Lebedev, Y. S.; Schlaepfer, W.; Merbach, A. E. Structural and Dynamic Parameters Obtained from ^{17}O NMR, EPR, and NMRD Studies of Monomeric and Dimeric Gd^{3+} Complexes of Interest in Magnetic Resonance Imaging: An Integrated and Theoretically Self-Consistent Approach ^{1}. *J. Am. Chem. Soc.* **1996**, *118* (39), 9333–9346. https://doi.org/10.1021/ja961743g.

(86) Lammers, H.; Maton, F.; Pubanz, D.; van Laren, M. W.; van Bekkum, H.; Merbach, A. E.; Muller, R. N.; Peters, J. A. Structures and Dynamics of Lanthanide(III) Complexes of Sugar-Based DTPA-Bis(Amides) in Aqueous Solution: A Multinuclear NMR Study. *Inorg. Chem.* **1997**, *36* (12), 2527–2538. https://doi.org/10.1021/ic961359k.

(87) Benelli, C.; Gatteschi, D. Magnetism of Lanthanides in Molecular Materials with Transition-Metal Ions and Organic Radicals. *Chem. Rev.* **2002**, *102* (6), 2369–2388. https://doi.org/10.1021/cr010303r.

(88) Botta, M.; Avedano, S.; Giovenzana, G. B.; Lombardi, A.; Longo, D.; Cassino, C.; Tei, L.; Aime, S. Relaxometric Study of a Series of Monoaqua GdIII Complexes of Rigidified EGTA-Like Chelators and Their Noncovalent Interaction with Human Serum Albumin. *Eur. J. Inorg. Chem.* **2011**, *2011* (6), 802–810. https://doi.org/10.1002/ejic.201001103.

(89) Lucio-Martínez, F.; Garda, Z.; Váradi, B.; Kálmán, F. K.; Esteban-Gómez, D.; Tóth, É.; Tircsó, G.; Platas-Iglesias, C. Rigidified Derivative of the Non-Macrocyclic Ligand H $_4$OCTAPA for Stable Lanthanide(III) Complexation. *Inorg. Chem.* **2022**, *61* (12), 5157–5171. https://doi.org/10.1021/acs.inorgchem.2c00501.

(90) Caravan, P.; Ellison, J. J.; McMurry, T. J.; Lauffer, R. B. Gadolinium(III) Chelates as MRI Contrast Agents: Structure, Dynamics, and Applications. *Chem. Rev.* **1999**, *99* (9), 2293–2352. https://doi.org/10.1021/cr980440x.

(91) Pintacuda, G.; Hohenthanner, K.; Otting, G.; Müller, N. Angular Dependence of Dipole-Dipole-Curie-Spin Cross-Correlation Effects in High-Spin and Low-Spin Paramagnetic Myoglobin∗. *J. Biomol. NMR* **2003**, *27*, 115–132.

(92) Willcott, M. R. MestRe Nova. *J. Am. Chem. Soc.* **2009**, *131* (36), 13180–13180. https://doi.org/10.1021/ja906709t.

(93) APEX3 Version 2016.1, Madison, Wisconsin, USA. *Bruker AXS Inc.* 2016.

(94) SAINT Version 8.37A; Bruker AXS Inc., 2015.

(95) Sheldrick, G. M. SADABS, Version 2.10, University of Göttingen, Germany, 2004.

(96) Sheldrick, G. M. Crystal Structure Refinement with *SHELXL*, Version 2014/5. *Acta Crystallogr. Sect. C Struct. Chem.* **2015**, *71* (1), 3–8. https://doi.org/10.1107/S2053229614024218.

(97) Sheldrick, G. M. A Short History of *SHELX*. *Acta Crystallogr. A* **2008**, *64* (1), 112–122. https://doi.org/10.1107/S0108767307043930.

(98) Frisch, M. J.; Trucks, G. W.; Schlegel, H. B.; Scuseria, G. E.; Robb, M. A.; Cheeseman, J. R.; Scalmani, G.; Barone, V.; Petersson, G. A.; Nakatsuji, H.; Li, X.; Caricato, M.; Marenich, A. V.; Bloino, J.; Janesko, B. G.; Gomperts, R.; Mennucci, B.; Hratchian, H. P.; Ortiz, J. V.; Izmaylov, A. F.; Sonnenberg, J. L.; Williams; Ding, F.; Lipparini, F.; Egidi, F.; Goings, J.; Peng, B.; Petrone, A.; Henderson, T.; Ranasinghe, D.; Zakrzewski, V. G.; Gao, J.; Rega, N.; Zheng, G.; Liang, W.; Hada, M.; Ehara, M.; Toyota, K.; Fukuda, R.; Hasegawa, J.; Ishida, M.; Nakajima, T.; Honda, Y.; Kitao, O.; Nakai, H.; Vreven, T.; Throssell, K.; Montgomery Jr., J. A.; Peralta, J. E.; Ogliaro, F.; Bearpark, M. J.; Heyd, J. J.; Brothers, E. N.; Kudin, K. N.; Staroverov, V. N.; Keith, T. A.; Kobayashi, R.; Normand, J.; Raghavachari, K.; Rendell, A. P.; Burant, J. C.; Iyengar, S. S.; Tomasi, J.; Cossi, M.; Millam, J. M.; Klene, M.; Adamo, C.; Cammi, R.; Ochterski, J. W.; Martin, R. L.; Morokuma, K.; Farkas, O.; Foresman, J. B.; Fox, D. J. Gaussian 16 Rev. C.01, 2016.

(99) Tao, J.; Perdew, J. P.; Staroverov, V. N.; Scuseria, G. E. Climbing the Density Functional Ladder: Nonempirical Meta–Generalized Gradient Approximation Designed for Molecules and Solids. *Phys. Rev. Lett.* **2003**, *91* (14), 146401. https://doi.org/10.1103/PhysRevLett.91.146401.

(100) Dolg, M.; Stoll, H.; Preuss, H. Energy- adjusted *Ab Inio* Pseudopotentials for the Rare Earth Elements. *J. Chem. Phys.* **1989**, *90* (3), 1730–1734. https://doi.org/10.1063/1.456066.

(101) Weigend, F.; Ahlrichs, R. Balanced Basis Sets of Split Valence, Triple Zeta Valence and Quadruple Zeta Valence Quality for H to Rn: Design and Assessment of Accuracy. *Phys. Chem. Chem. Phys.* **2005**, *7* (18), 3297–3305. https://doi.org/10.1039/b508541a.

(102) Tomasi, J.; Mennucci, B.; Cancès, E. The IEF Version of the PCM Solvation Method: An Overview of a New Method Addressed to Study Molecular Solutes at the QM Ab Initio Level. *J. Mol. Struct. THEOCHEM* **1999**, *464* (1–3), 211–226. https://doi.org/10.1016/S0166-1280(98)00553-3.

(103) Tomasi, J.; Mennucci, B.; Cammi, R. Quantum Mechanical Continuum Solvation Models. *Chem. Rev.* **2005**, *105* (8), 2999–3094. https://doi.org/10.1021/cr9904009.

(104) Malmqvist, P.-Å.; Roos, B. O. The CASSCF State Interaction Method. *Chem. Phys. Lett.* **1989**, *155* (2), 189–194. https://doi.org/10.1016/0009-2614(89)85347-3.

(105) Neese, F. The ORCA Program System. *WIREs Comput. Mol. Sci.* **2012**, *2* (1), 73–78. https://doi.org/10.1002/wcms.81.

(106) Neese, F. Software Update: The ORCA Program System, Version 4.0. *WIREs Comput. Mol. Sci.* **2018**, *8* (1), e1327. https://doi.org/10.1002/wcms.1327.

(107) Aravena, D.; Neese, F.; Pantazis, D. A. Improved Segmented All-Electron Relativistically Contracted Basis Sets for the Lanthanides. *J. Chem. Theory Comput.* **2016**, *12* (3), 1148–1156. https://doi.org/10.1021/acs.jctc.5b01048.

(108) Neese, F. An Improvement of the Resolution of the Identity Approximation for the Formation of the Coulomb Matrix. *J. Comput. Chem.* **2003**, *24* (14), 1740–1747. https://doi.org/10.1002/jcc.10318.

(109) Izsák, R.; Neese, F. An Overlap Fitted Chain of Spheres Exchange Method. *J. Chem. Phys.* **2011**, *135* (14), 144105. https://doi.org/10.1063/1.3646921.

(110) Stoychev, G. L.; Auer, A. A.; Neese, F. Automatic Generation of Auxiliary Basis Sets. *J. Chem. Theory Comput.* **2017**, *13* (2), 554–562. https://doi.org/10.1021/acs.jctc.6b01041.

(111) Reiher, M. Douglas–Kroll–Hess Theory: A Relativistic Electrons-Only Theory for Chemistry. *Theor. Chem. Acc.* **2006**, *116* (1–3), 241–252. https://doi.org/10.1007/s00214-005-0003-2.

(112) Barysz, M.; Sadlej, A. J. Two-Component Methods of Relativistic Quantum Chemistry: From the Douglas–Kroll Approximation to the Exact Two-Component Formalism. *J. Mol. Struct. THEOCHEM* **2001**, *573* (1–3), 181–200. https://doi.org/10.1016/S0166-1280(01)00542-5.

(113) Visscher, L.; Dyall, K. G. Dirac–Fock Atomic Electronic Structure Calculations Using Different Nuclear Charge Distributions. *At. Data Nucl. Data Tables* **1997**, *67* (2), 207–224. https://doi.org/10.1006/adnd.1997.0751.

(114) Maganas, D.; Sottini, S.; Kyritsis, P.; Groenen, E. J. J.; Neese, F. Theoretical Analysis of the Spin Hamiltonian Parameters in $Co^{(II)}S_4$ Complexes, Using Density Functional Theory and Correlated Ab Initio Methods. *Inorg. Chem.* **2011**, *50* (18), 8741–8754. https://doi.org/10.1021/ic200299y.

(115) Atanasov, M.; Aravena, D.; Suturina, E.; Bill, E.; Maganas, D.; Neese, F. First Principles Approach to the Electronic Structure, Magnetic Anisotropy and Spin Relaxation in Mononuclear 3d-Transition Metal Single Molecule Magnets. *Coord. Chem. Rev.* **2015**, *289–290*, 177–214. https://doi.org/10.1016/j.ccr.2014.10.015.

(116) Marenich, A. V.; Cramer, C. J.; Truhlar, D. G. Universal Solvation Model Based on Solute Electron Density and on a Continuum Model of the Solvent Defined by the Bulk Dielectric Constant and Atomic Surface Tensions. *J. Phys. Chem. B* **2009**, *113* (18), 6378–6396. https://doi.org/10.1021/jp810292n.

TOC Graphic

To be done!!

Synopsis: XXXXXXXXXXXXXXXXXXXXXXXXXXXXXXX